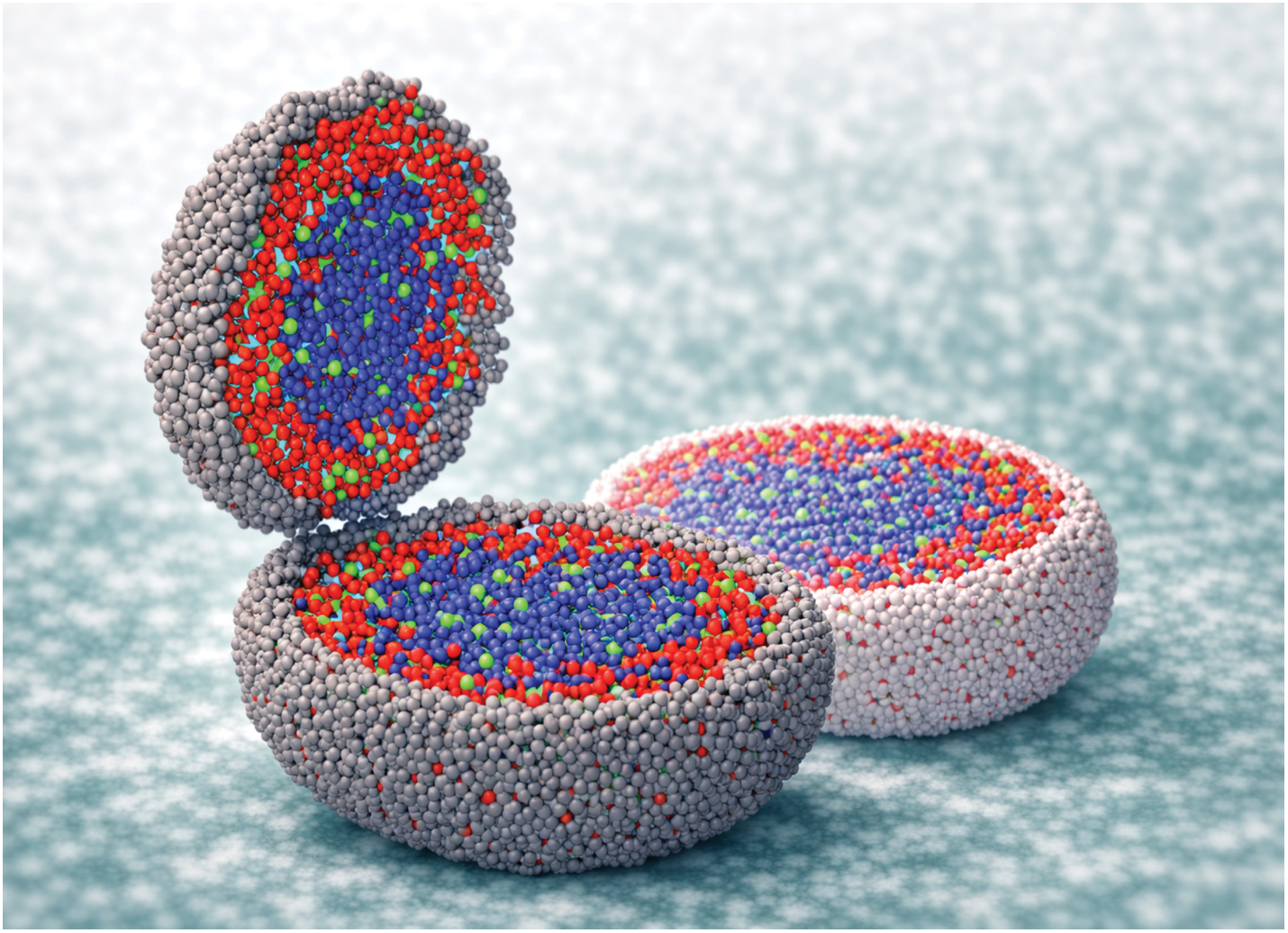

Highlighting research from the J. M. Schwarz Theory Group, Department of Physics, Syracuse University.

Differential crosslinking and contractile motors drive nuclear chromatin compaction

Using simulations, we show how differential chromatin crosslinking and contractile motors reorganize nuclear chromatin, driving segregation with euchromatin in the interior and heterochromatin enriched at the periphery, linking chromatin compaction to nuclear deformations.

Image reproduced by permission of Ligesh Theeyancheri, Edward J. Banigan and J. M. Schwarz from *Soft Matter*, 2026, **22**, 1326.

As featured in:

See Ligesh Theeyancheri, Edward J. Banigan and J. M. Schwarz, *Soft Matter*, 2026, **22**, 1326.

ROYAL SOCIETY OF CHEMISTRY

rsc.li/soft-matter-journal

Registered charity number: 207890

Soft Matter

PAPER

View Article Online
View Journal | View Issue

Cite this: *Soft Matter*, 2026, **22**, 1326

Differential crosslinking and contractile motors drive nuclear chromatin compaction

Ligesh Theeyancheri, *[a] Edward J. Banigan *[b] and J. M. Schwarz*[ac]

During interphase, the cell nucleus exhibits spatial compartmentalization between transcriptionally active euchromatin and transcriptionally repressed heterochromatin. In conventional nuclear organization, euchromatin is enriched in the nuclear interior, while heterochromatin – approximately 50% denser – resides near the periphery. The nuclear lamina, a deformable structural shell, further modulates peripheral chromatin organization. Here, we investigate a chromatin model in which an active, crosslinked polymer is tethered to a deformable lamina shell. We show that contractile motor activity, shell deformability, and the spatial distribution of crosslinks jointly determine compartmentalization. Specifically, a radial crosslink density gradient, even with a small increase toward the periphery, coupled with motor activity, drives genomic segregation consistent with experimental observations. This effect arises as motors preferentially draw crosslinks toward the periphery, forming dense domains that promote heterochromatin formation. Our model also predicts increased stiffness of nuclear wrinkles due to heterochromatin compaction beneath the lamina, consistent with instantaneous stiffening observed under nanoindentation. We conclude by outlining potential experimental approaches to validate our model predictions.

Received 9th August 2025,
Accepted 3rd December 2025

DOI: 10.1039/d5sm00812c

rsc.li/soft-matter-journal

I. Introduction

The cell nucleus plays a vital role in eukaryotic cells by enclosing and safeguarding genetic information encoded within chromatin polymer fibers composed of DNA and histone proteins.[1,2] Collectively, these polymer fibers constitute spatially partitioned chromatin states within the nucleus, broadly known as euchromatin and heterochromatin. Euchromatin is the gene-rich, transcriptionally active, and loosely packed form, while heterochromatin is gene-poor, transcriptionally inactive, and densely packed.[3,4] In conventional nuclear organization, euchromatin resides in the nuclear interior, while heterochromatin is localized at the nuclear periphery,[3–5] with a density difference of 50% or more between the two.[6,7]

Recent studies suggest several plausible explanations for spatial segregation of peripheral heterochromatin and interior euchromatin concentrated in the inner nuclear region. There is substantial evidence that compartmentalization of the genome can result from mesoscale phase separation,[8–21] with peripheral heterochromatin maintained by attractive interactions with the lamina.[15,19,22,23] Additional simulations indicate that compartmentalization can be obtained by such affinity interactions, even when chromatin is not programmed as either hetero- or euchromatin *a priori*.[24–27] Besides affinity-mediated interactions, differences in the other physical properties of heterochromatin and euchromatin may also contribute to their partitioning.[28,29] Nuclear elastography measurements indicate that heterochromatin may be almost four times stiffer than euchromatin;[30] simulations predict that conventional chromatin organization can be obtained either by increasing the bending stiffness of the heterochromatin relative to euchromatin.[14,31–34] Entropic effects from nonspecific protein binding may further contribute to chromatin compaction, clustering, and compartmentalization.[35,36] In addition to equilibrium effects, a number of studies suggest that compartmentalization of the genome can result from nonequilibrium mesoscale phase separation driven by heterogeneous activity.[37–46] Similarly, confined active ring polymers models, with active and passive segments at different effective temperatures, can form topologically constrained, dynamically arrested domains and exhibit microphase separation with coherent motion of active regions, providing a minimal nonequilibrium physical analogy to chromatin compartmentalization.[47,48]

While a nonequilibrium phase separation approach may provide a basis for chromatin compartmentalization, as the cell nucleus is an out-of-equilibrium system, chromatin and the nucleus also exhibit highly nontrivial dynamics. Specifically,

[a] *Physics Department, Syracuse University, Syracuse, NY 13244, USA. E-mail: ligeshbhaskar@gmail.com, jmschw02@syr.edu*
[b] *Institute of Medical Engineering & Science and Department of Physics, Massachusetts Institute of Technology, Cambridge, MA 02139, USA. E-mail: ebanigan@mit.edu*
[c] *Indian Creek Farm, Ithaca, NY 14850, USA*

several experiments observe micron-scale correlated movement of genomic regions over seconds.[49–55] This correlated motion is reduced in the absence of ATP or by reduction of activity by the motors, such as transcribing RNA polymerases.[49,50,53,56] At the same time, the deformable lamina shell exhibits a broadly distributed power spectrum.[57] It has been demonstrated that both the correlated chromatin motion and the power spectrum can be quantitatively understood with an active, crosslinked polymeric system confined within a deformable shell.[58] These correlated motions are thought to drive dynamic nuclear shape deformations, such as wrinkles, bulges, and ''blebs'', or chromatin-filled nuclear protrusions that are prone to rupture.[59,60] Given these findings, we ask how much of the dynamic architecture of the cell nucleus can be accounted for by active polymer physics. Specifically, is motor activity combined with connectivity within chromatin sufficient to compartmentalize chromatin into different forms, particularly euchromatin and heterochromatin?

Here, we report progress towards answering this question to arrive at a simple, novel biophysical mechanism for chromatin compartmentalization based on motor activity and varying spatial profiles of chromatin crosslinking. Various molecular motors and enzymes operate throughout chromatin, including RNA polymerase II and cohesin.[61,62] Likewise, DNA- and chromatin-binding proteins can act as crosslinkers by bridging chromatin sites. In particular, heterochromatin protein 1 (HP1) is a crucial mediator of chromatin crosslinking and is found in both heterochromatin and euchromatin.[63–68] HP1's diverse roles, including heterochromatin formation, gene silencing, telomere maintenance, DNA replication, and repair, suggest that the interactions of HP1 with neighboring protein complexes may play a significant role in regulating its ability to crosslink chromatin. Therefore, the localization of other protein complexes, such as Cullin 4B (CUL4B), interacting with HP1 could give rise to a spatially varying distribution of crosslinks within the nucleus.[69]

Given this biological context, our model incorporates simple extensile and contractile monopolar motor activities, representative of ATP-driven processes in the nucleus.[56,58,59,70] We also implement chromatin crosslinks that mimic chromatin-binding proteins like HP1.[63,65,66,71] To capture the effects of differential HP1 localization in the nucleus, we vary the spatial distribution of crosslinks using uniform, linear, and inverted radial crosslink profiles. Additionally, our model accounts for the deformable nature of the nuclear envelope, as the lamina is soft and undergoes shape fluctuations.[57,58,72,73] We hypothesize that patterning of physical constraints within chromatin may regulate chromatin spatial organization, while also facilitating mechanoresponses and dynamic adaptation of the nucleus and genome to internal and external perturbations.[2,66,73–80]

II. Model

The chromatin–lamina system is modeled with the chromatin represented as a Rouse-like chain and the lamina as an elastic, polymeric shell, with linkages between the chain and the shell.[58,81,82] More specifically, monomers in the lamina shell are connected by Hookean springs with spring constant K. In the initial preparation of the shell, a Fibonacci sphere with 5000 nodes is generated and 5000 identical monomers are placed at these nodes. The monomers connected by springs form a mesh with an average coordination number of 4.5. The monomers have soft-core repulsive interactions to model excluded volume. The chromatin fiber, on the other hand, is modeled by a Rouse-like chain with soft-core repulsion between each monomer, which has radius $r_p = 0.43089$. A three-dimensional self-avoiding random walk in an FCC lattice is performed to generate the polymer with $N = 5000$ monomers. This coarse-grained simplification focuses on mesoscale interactions within a chromosome territory, which dominate at the spatial and temporal scales relevant for chromatin compartmentalization. Single-polymer frameworks of this kind have been widely used to capture key physical features of interphase nuclear organization.[10,23–25,37,45,46,58,59,70] The chromatin polymer is then packed in a hard spherical shell before equilibration. The monomers of the shell have the same physical properties as the chain monomers in terms of size (r_s) and spring constant.

Initial configurations of the lamina and the chromatin confined within are generated using the following protocol.[58] The spherical shell is gradually shrunk by moving its monomers inward, which in turn drives the chain monomers inward due to soft-core repulsions. Once the target radius is reached, the positions of the shell monomers are relaxed, and the spring lengths are updated to finalize the initial system configuration (Fig. S1). With the initial shell radius, $R_s = 10$, the corresponding nuclear volume fraction is defined as, $\phi_{\text{nucleus}} = \dfrac{N \times \frac{4}{3}\pi {r_p}^3}{\frac{4}{3}\pi {R_s}^3}$, where N is the number monomers of chromatin chain, r_p is the monomer radius. This yields an initial volume fraction of $\phi_{\text{nucleus}} \approx 0.4$ prior to further relaxation. We repeat this process and generate 50 initial configurations. We define the simulation units such that one unit of length corresponds to 1 μm, one unit of time is 0.5 seconds (chosen to provide a physically realistic correspondence between simulation and experimental dynamics while maintaining numerical stability), and the energy scale is $k_B T = 10^{-21}$ J, where $T = 300$ K (a complete list of simulation parameters is provided in the SI (Table S1)).

We implement the excluded volume interactions using a repulsive, soft-core potential between any two monomers, i and j, which are separated by a distance $|\vec{r}_{ij}|$, modeled using:

$$V_{\text{Ex}}(r_{ij}) = \begin{cases} \frac{1}{2}K_{\text{Ex}}\left(|r_{ij}| - \sigma_{ij}\right)^2 & \text{if } |r_{ij}| < \sigma_{ij}, \\ 0 & \text{otherwise,} \end{cases} \quad (1)$$

where $\sigma_{ij} = r_{p_i} + r_{p_j}$. We also incorporate crosslinks in chromatin,[66] tethering of chromatin to the lamina, and motor activity within the chromatin polymer (Fig. 1). We establish a total of N_c crosslinks in the chromatin by adding springs

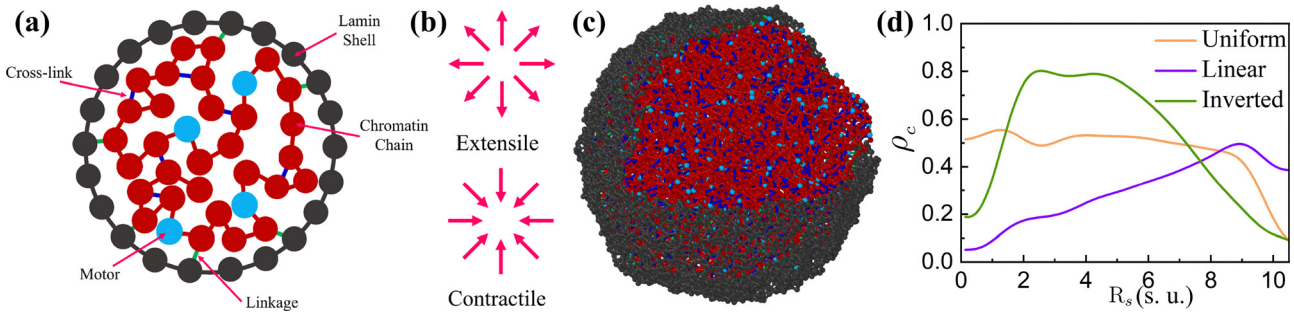

Fig. 1 3D computational model of chromatin in a deformable nucleus. (a) A two-dimensional schematic of the model. (b) A schematic illustrating the two types of motors acting on the chromatin. (c) A Simulation snapshot. The chromatin polymer consists of linearly connected monomers, depicted in red, while the active chromatin subunits are shown in cyan. The lamina is made up of lamin subunits, represented in grey. (d) The radial distribution of crosslink density (ρ_c) as a function of nuclear radius R_s. All quantities are reported in simulation units (s.u.), where 1 s.u. of length = 1 μm.

between randomly selected pairs of polymer monomers, where the springs have the same stiffness, K, as those connecting adjacent monomers along the polymer chain. A crosslink may be established if the distance between the selected monomers is less than $r_{link} = 3r_p$.

To investigate how the distribution of crosslinks influences the spatial organization of chromatin within the nucleus, we consider three distinct (initial) crosslinking profiles: uniform, linear, and inverted (Fig. 1d). These profiles are biologically motivated by the possibility that HP1-CUL4B mediated interactions locally modulate chromatin crosslinking, leading to spatial variations in crosslink density within the nucleus. In the uniform profile, crosslinks are formed randomly between any N_c pairs of monomers. The linear profile involves a linearly increasing crosslink density from the center of the nucleus toward the nuclear periphery. Conversely, in the inverted profile, the crosslink density increases linearly from the nuclear periphery toward the center of the nucleus. Crosslinks are assigned at the start of the simulation by dividing the nucleus into concentric spherical shells of equal volume and assigning a radial probability distribution for crosslink formation across these shells. Each shell spans an interval $[r_{shell}(i), r_{shell}(i+1)]$, and its radial position is defined as $r^i_{shell} = \frac{r^{i,inner}_{shell} + r^{i,outer}_{shell}}{2}$. For the ith shell, the probability of forming a crosslink is proportional to $\frac{r^i_{shell}}{R_s}$ for the linear profile or $1 - \frac{r^i_{shell}}{R_s}$ for the inverted profile, where r^i_{shell} denotes the radial position of the ith spherical shell in the radial direction and R_s is the nuclear radius. Crosslinks are initialized once at the start of the simulation and remain topologically fixed throughout, although their spatial configuration evolves dynamically. The slope of the radial crosslinking profile remains fixed across simulations with different total numbers of crosslinks. This framework allows us to analyze how different spatial distributions and concentrations of crosslinks affect the three-dimensional arrangement of chromatin inside the nucleus.

A total of N_L random polymer-shell linkages are introduced to model connections between chromatin and the nuclear lamina.[79,83,84] In addition to thermal fluctuations, we incorporate motor activity by designating N_m chromatin monomers as active.[58,59] An active monomer exerts a force $\boldsymbol{F_a} = \pm f_m \hat{r}_{ij}$ on surrounding monomers within a spatial cutoff distance $M_{range} = 3r_p$, where $r_p = 0.43089$ is the chromatin monomer radius. f_m denotes the strength of the motor force. The motors can exert either extensile or contractile forces, pushing the monomers apart or drawing them together (Fig. 1b), analogous to other models that explicitly account for motor activity.[56,70] A motor stochastically unbinds from a monomer with characteristic turnover time, $\tau_m = 20$, after which the monomer becomes passive and the motor binds to another randomly selected chromatin monomer, which will then exert active forces. Our model does not impose predefined active regions or domain-specific properties. Instead, chromatin monomers randomly switch between active and passive states with this turnover time, capturing spatially distributed ATP-dependent motor activity. In this coarse-grained framework, active monomers represent generic ATP-driven processes-including transcription, remodeling, and cohesin activity, distributed throughout the nucleus. Although loop extrusion is not modeled explicitly, its large-scale mixing effects are implicitly captured, consistent with experiments showing ATP-dependent chromatin motion across both dense and open regions.[28,49,54] The timescale $\tau_m \approx 10$ s is comparable to the timescale of experimentally observed chromatin motions.[49,50]

The system evolves through Brownian dynamics, governed by the overdamped equations of motion:

$$\xi \dot{\boldsymbol{r}}_i = \boldsymbol{F_{Ex}} + \boldsymbol{F_{Sp}} + \boldsymbol{F_{Th}} + \boldsymbol{F_{Ac}}, \quad (2)$$

where $\boldsymbol{r}_i$ represents the position of the ith monomer at time t, and ξ is the friction coefficient, which is related to the thermal Gaussian noise, *via* the fluctuation–dissipation theorem. $\boldsymbol{F_{Ex}}$ represents the force arising from excluded volume interactions, $\boldsymbol{F_{Sp}}$ accounts for the harmonic forces generated by polymer chain springs, chromatin crosslink springs, and chromatin–lamina linkage springs, $\boldsymbol{F_{Th}}$ corresponds to thermal forces, and $\boldsymbol{F_{Ac}}$ denotes the force due to the contractile or extensile motors. For the passive system, no motors are present, and the active force $\boldsymbol{F_{Ac}}$ is set to zero. We employ the Euler–Maruyama method for time integration, with a time step of $d\tau = 10^{-4}$, and a total simulation time of $\tau = 10^3$. To evaluate the structural properties in the steady state, we measure the radius of gyration, R_g, and

average radius of the lamina shell, $\langle R_s \rangle$. The system is considered to be in steady state when these quantities no longer exhibit significant changes over time (Fig. S2).

III. Results

As we consider different types of motors and different crosslinking profiles, we also use a reference configuration, the chromatin distribution in the absence of both crosslinks and chromatin–lamina linkages, as well as in systems with lamina linkages but no crosslinks (Fig. S3). Without chromatin–lamina linkages (Fig. S3a), chromatin is locally depleted near the lamina due to soft repulsion and exhibits a mild bias toward the nuclear interior, particularly in the presence of contractile activity. When lamina linkages are introduced (Fig. S3b), the chromatin distribution becomes nearly uniform. This result suggests that chromatin–lamina linkages are essential to prevent excess accumulation of chromatin in the interior. In the following subsections, we systematically analyze how these molecular motors and crosslinks can establish conventional heterochromatin–euchromatin organization inside the nucleus.

A. Radial chromatin distribution governed by motor activity and crosslink profile

To quantify the effect of the crosslink distribution on the radial chromatin density, ϕ_c, we compute ϕ_c by dividing the nuclear volume into concentric shells of equal width, counting the number of chromatin monomers in each shell, and normalizing by shell volume. Fig. 2 depicts ϕ_c *vs.* radial position, R_s, for both initial configurations and steady states across passive, extensile, and contractile motor conditions with varying crosslink profiles. The initial chromatin distribution in the nucleus is uniform regardless of the crosslink density profile, as shown in Fig. 2a. As the system evolves, chromatin spatial organization changes in response to the interplay of crosslinks and motor activity.

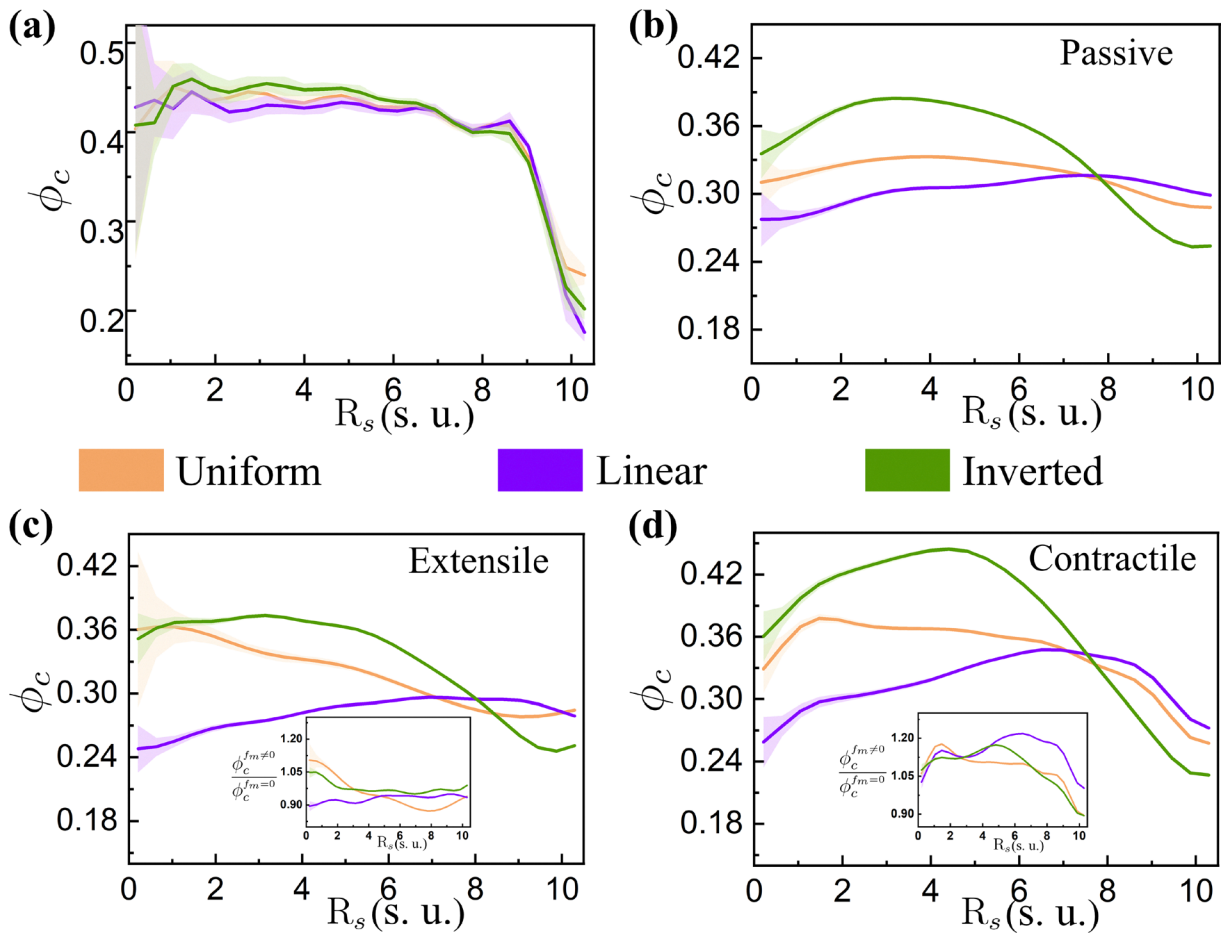

Fig. 2 Radial chromatin density shaped by motors and crosslink profiles. Chromatin density, ϕ_c, as a function of R_s. (a) Initial chromatin density at t = 0, and final chromatin density for (b) passive, (c) extensile, and (d) contractile motors, for different crosslink density profiles. The rescaled chromatin density, $\frac{\phi_c^{fm\neq0}}{\phi_c^{fm=0}}$, is shown in the insets of panels (c) and (d), highlighting motor-induced changes relative to the passive case. Each case corresponds to N_c = 2000 crosslinks and N_L = 600 chromatin–lamina linkages. All quantities are reported in simulation units (s.u.), where 1 s.u. of length = 1 μm and 1 s.u. of time = 0.5 s. The shaded regions represent the standard error of the mean, calculated over 50 independent configurations.

To distinguish the contribution of motor activity, we first examine the passive case without motors, where density profiles depend on the crosslink distribution. The uniform and linear crosslink profiles yield homogeneously distributed chromatin across R_s, while the inverted crosslink profile generates higher chromatin density in the nuclear interior (Fig. 2b).

Motor activity alters the spatial pattern of chromatin density, depending on the crosslink distribution. Upon introducing extensile motors, chromatin localizes more toward the center in simulations with uniform and inverted crosslink density profiles. In contrast, with linear crosslink profiles, we observe a nearly uniform chromatin distribution as a function of R_s, with slightly elevated chromatin concentration at the periphery (Fig. 2c). Notably, implementing contractile motors dramatically alters chromatin distribution across all three crosslink profiles. Uniform and inverted crosslink profiles lead to higher chromatin accumulation in the nuclear interior, with the inverted profile showing preferentially higher interior accumulation compared to the uniform profile. Strikingly, the linear crosslink profile results in significantly higher chromatin accumulation at the nuclear boundary (Fig. 2d). This chromatin density profile resembles the conventional spatial distribution of chromatin observed in many differentiated cells[3,5] in that denser heterochromatin-like regions are near the nuclear periphery while less dense euchromatin-like chromatin is localized in the interior.

We also compare the spatial variation of chromatin density in the presence of motors to that in the corresponding passive system by examining the chromatin density scaled by the passive case, given as $\frac{\phi_c^{f_m\neq 0}}{\phi_c^{f_m=0}}$ (insets in Fig. 2c and d), where $\phi_c^{f_m\neq 0}$ and $\phi_c^{f_m=0}$ denote the chromatin densities with and without (passive case) motor activity, respectively. This reveals that extensile motors generally lead to chromatin decompaction, whereas contractile motors result in significant chromatin compaction, particularly in the case of a linear crosslink profile. Additionally, we vary the number of motors N_m for the linear crosslink density profile case. Reducing the number of contractile motors decreases the extent of chromatin compaction, while reducing extensile motors yields less decompaction relative to higher motor numbers (Fig. S4). Our simulations demonstrate that motor activity, combined with nonuniformity in the spatial distribution of crosslinks, can alter the spatial distribution of chromatin. In particular, the synergistic action of contractile motors and a linearly increasing radial profile of crosslinks is sufficient to recapitulate the conventional nuclear architecture, suggesting a novel biophysical mechanism for the establishment of chromatin segregation patterns *in vivo*.

Subsequently, we examine how chromatin distribution changes for different total number, N_c, of crosslinks in the system, while maintaining a linear crosslink profile. Fig. 3 illustrates the effects across passive, extensile, and contractile motor conditions. Our findings reveal that chromatin compaction intensifies with increasing crosslink numbers, N_c, irrespective of motor activity. However, the magnitude of this effect varies markedly between different motor types. The passive and extensile cases (Fig. 3a and b) demonstrate modest enhancement in chromatin density as N_c increases, whereas the contractile case (Fig. 3c) manifests substantially greater chromatin compaction. Among all three cases, extensile motors yield the least chromatin compaction because their activity locally expands chromatin. The absence of motor activity enables intermediate levels of compaction with increasing N_c, as expected from entropic considerations. Contractile motors induce the highest degree of overall chromatin compaction. Notably, the chromatin density is significantly enhanced at the nuclear periphery, reinforcing the conventional chromatin distribution pattern observed in experiments.[3,5] Additionally, increasing the number of chromatin–lamina linkages reinforces the spatial variation of chromatin density, leading to reduced density in the nuclear interior and accumulation near the periphery (Fig. S5). Our results establish that motor activity can focus spatial inhomogeneities in crosslinking into spatial patterning of chromatin polymer density. Contractile motor activity dramatically amplifies crosslink-dependent peripheral compaction, suggesting a general physical mechanism for regulating chromatin architecture through the interplay of molecular motors with the physical constraints on chromatin in the nucleus.

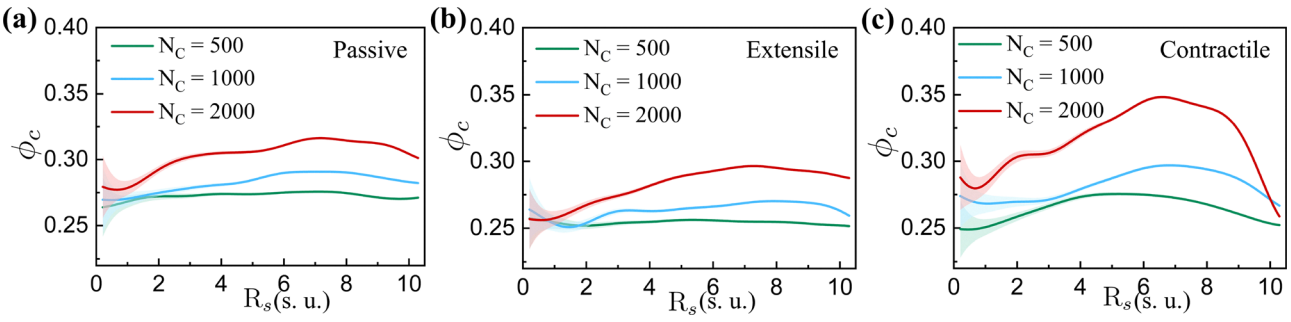

Fig. 3 Influence of motor activity and number of crosslinks on chromatin distribution. Chromatin density, ϕ_c, as a function of R_s for (a) passive, (b) extensile, and (c) contractile motors, shown for different numbers of crosslinks (N_c) with a linear crosslink density profile. Results correspond to N_L = 600 chromatin crosslinks. All quantities are reported in simulation units (s.u.), where 1 s.u. of length = 1 μm and 1 s.u. of time = 0.5 s. The shaded regions represent the standard error of the mean, calculated over 50 independent configurations.

B. Spatial segregation of euchromatin and heterochromatin contributes to overall chromatin density patterns

To quantify the observed patterns of chromatin architecture in our model, we sought to identify euchromatin-like and heterochromatin-like contributions to the spatial distribution of chromatin density. We focused on the simulations employing linear crosslink profiles with contractile motors, as this condition generates chromatin distributions that most closely resemble conventional chromatin organization.[3,5] In our model, euchromatin and heterochromatin-like domains emerge dynamically from the synergistic effects of motor activity, crosslink heterogeneity, and confinement, consistent with earlier polymer modeling approaches where chromatin compartmentalization arises intrinsically without preassigning euchromatin or heterochromatin identities.[24–27,35]

To differentiate the radial chromatin density into euchromatin and heterochromatin components, we classified chromatin loci by local chromatin density. For each chromatin monomer i, we compute the local density ϕ^i_{local} as the total chromatin volume within a spherical neighborhood of radius R_{EH} centered on the ith monomer, divided by the volume of the sphere (Fig. 4a). Monomers with $\phi^i_{\text{local}} > \phi_{\text{cut}}$ (where ϕ_{cut} represents 95% of the total chromatin density) are categorized as heterochromatin (HetCh), while the remaining monomers are classified as euchromatin (EuCh) (Fig. 4a). The resulting density profiles of heterochromatin and euchromatin with a linear crosslink configuration are plotted as a function of the nuclear radius, R_s, in Fig. 4b, revealing distinct, spatially segregated chromatin domains. We observe that heterochromatin is preferentially localized at the nuclear periphery, while euchromatin predominantly occupies the nuclear interior, a spatial arrangement that aligns with previously reported chromatin organization patterns.[3,5] In contrast to the contractile motor scenario, the passive and extensile cases exhibit a radial chromatin density profile that is predominantly shaped by euchromatin, with heterochromatin contributing less to the overall density throughout the nucleus (Fig. S6). This highlights that the interplay between crosslink distribution and motor activity could be a fundamental mechanism driving the characteristic spatial segregation and differential compaction of euchromatin and heterochromatin domains in the cell nucleus.

To further assess spatial chromatin compartmentalization, we compute the mean local densities of euchromatin and heterochromatin, $\langle \phi^c_{\text{local}} \rangle$. The average local densities are $\langle \phi^c_{\text{local}}(E) \rangle \approx 0.27$ for euchromatin and $\langle \phi^c_{\text{local}}(H) \rangle \approx 0.44$ for heterochromatin (Fig. 4c). The resulting density ratio, $\frac{\langle \phi^c_{\text{local}}(H) \rangle}{\langle \phi^c_{\text{local}}(E) \rangle} \approx 1.6$, quantifies the degree of chromatin compaction, which is aligned with experimental reports of a 50% density increase in heterochromatin relative to euchromatin.[6]

We next characterize the dynamics of the euchromatin and heterochromatin using mean square displacement of monomers, defined as $\overline{\Delta r_i^2(\tau)} = \frac{1}{T'-\tau}\int_0^{T'-\tau}[\mathbf{r}_i(t+\tau) - \mathbf{r}_i(t)]^2 \mathrm{d}t$, where $\mathbf{r}_i(t)$ denotes the position of the ith monomer at time t, T' is the total run time, and τ is the lag time (*i.e.*, the time window over which displacements are averaged along a trajectory). To obtain the time-and-ensemble-averaged MSD, we compute the average, $\left\langle \overline{\Delta r^2(\tau)} \right\rangle = \frac{1}{N'}\sum_{i=1}^{N'} \overline{\Delta r_i^2(\tau)}$, where N' represents the number of independent trajectories. We observe that euchromatin displays slightly faster dynamics than heterochromatin (Fig. S7), aligning with the trends noted in prior numerical[40,85] and experimental[86–88] work.

C. Radial distribution of motors and the associated number of crosslinks per motor regulate chromatin compaction

The 3D structure of chromatin within the nucleus in our simulations arises from the interplay between mechanical constraints imposed by crosslinks and active, motor-driven processes that dynamically reorganize chromatin. To understand how motor forces and structural connectivity influence chromatin compaction and spatial arrangement, we characterize the radial distribution of motors and the density distribution of crosslinks that they establish throughout the nuclear volume.

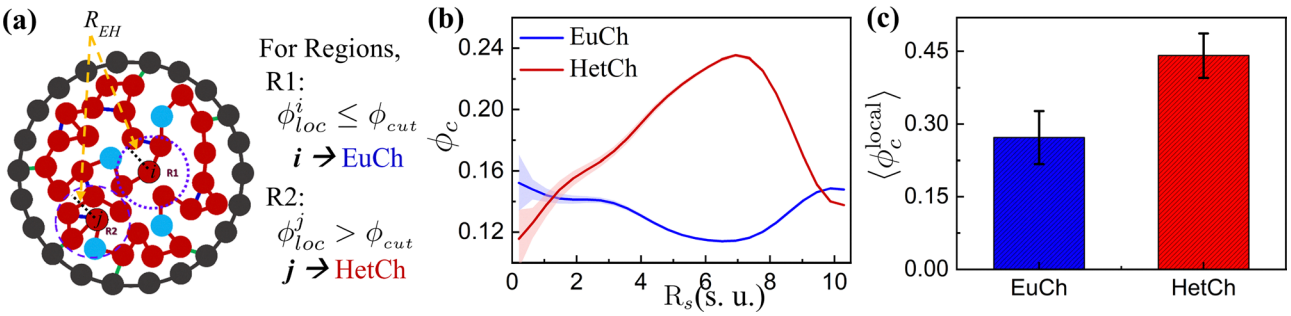

Fig. 4 Contractile motor-induced organization of euchromatin and heterochromatin. (a) Schematic illustrating the categorization of chromatin monomers into euchromatin (EuCh) and heterochromatin (HetCh) based on a local density cutoff (ϕ^{ij}_{loc}). (b) Density of EuCh and HetCh as a function of R_s and (c) average local density ($\langle \phi_c^{\text{local}} \rangle$) of EuCh and HetCh for a contractile motor with a linear crosslink density profile. The results shown correspond to N_c = 2000 crosslinks and N_L = 600 chromatin–lamina linkages. All quantities are reported in simulation units (s.u.), where 1 s.u. of length = 1 μm and 1 s.u. of time = 0.5 s. The shaded regions in panel (b) and error bars in panel (c) represent the standard error of the mean, calculated over 50 independent configurations.

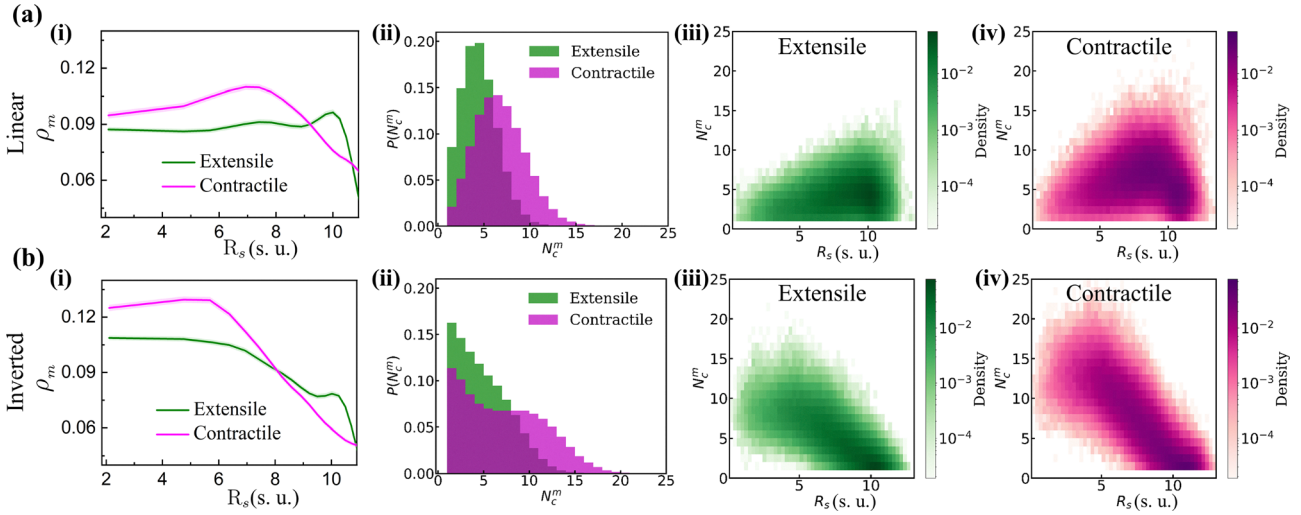

Fig. 5 Distribution of motor density and motor–crosslink associations for linear and inverted crosslink profiles. Radial distribution of (i) motor density (ρ_m) and (ii) the average number of crosslinks per motor. Density color map of the number of crosslinks per motor (N_c^m) as a function of R_s for (iii) extensile and (iv) contractile motors. (a) Linear and (b) inverted crosslink profiles, each with subpanels (i)–(iv). The results shown correspond to N_c = 2000 crosslinks and N_L = 600 chromatin–lamina linkages. All quantities are reported in simulation units (s.u.), where 1 s.u. of length = 1 μm and 1 s.u. of time = 0.5 s. The shaded regions in panel a represent the standard error of the mean, calculated over 50 independent configurations.

Therefore, we calculate the spatial distribution of motors, ρ_m, and number of crosslinks per motor, N_c^m, followed by the density mapping of N_c^m as a function of normalized radial position, R_s. In Fig. 5(a) and (b), we compare results for the linear and inverted crosslink profiles. To measure ρ_m, we count the number of motors in each of a set of equal volume concentric spherical shells dividing the nuclear volume, with the nuclear center at each time point determined by the mean position of the lamina monomers. To quantify number of crosslinks, N_c^m, for each motor monomer, we examine each motor's local environment within a cutoff volume of radius $3r_p$ (r_p is the radius of chromatin monomers) and count the number of crosslinked chromatin monomers within this sphere. This directly measures the average local crosslinking density, $P(N_c^m)$, associated with each motor (Fig. 5(a) and (b)(ii)). Furthermore, to understand the spatial dependence of crosslinks per motor, we map N_c^m as a function of radial position, R_s, by binning motors according to their distance from the nuclear center and calculating the number of crosslinks per motor within each bin. This analysis reveals how crosslinking density varies across the nuclear volume and correlates with motor distribution patterns (Fig. 5a and b(iii), (iv)).

The radial distribution of motor density, ρ_m, reveals distinct spatial organization patterns for extensile and contractile motors depending on the crosslink density profile. For a linear crosslink profile, extensile motors show a relatively uniform density with a slight peripheral increase, whereas contractile motors peak in the outer regions and drop near the boundary (Fig. 5a(i)). On the other hand, for an inverted crosslink profile, both motor types are enriched in the nuclear interior and decrease toward the periphery, with contractile motors exhibiting higher densities than extensile motors across R_s (Fig. 5b(i)). As expected, these motor distribution patterns correlate with the overall chromatin density distribution (Fig. 2c and d). However, there are some differences between the motor and chromatin density distributions, indicating that motion of motors (and likely, the surrounding chromatin) is important in maintaining the nonuniform spatial distribution of chromatin.

Furthermore, analysis of N_c^m distributions uncovers striking differences between the two crosslink profiles. In the linear profile, contractile motors show a marked increase in crosslinks per motor compared to extensile motors, evident from the rightward shift of the $P(N_c^m)$ peak (Fig. 5a(ii)). The inverted profile, in contrast, maintains a consistent peak location for both extensile and contractile motors, but with a much broader distribution of crosslinks per contractile motor than crosslinks per extensile motor (Fig. 5b(ii)). Thus, in both cases, contractile motors exhibit an ability to recruit highly connected chromatin, which could facilitate local increases in chromatin density.

The density map further substantiates these observations. In the case of the linear crosslink profile, the motors with the highest number, N_c^m, of crosslinks are predominantly localized to the nuclear periphery, with particular peripheral enrichment for contractile motors (Fig. 5a(iii) and (iv)). This pattern is opposite in the inverted crosslink configuration, where motors with higher crosslink densities are fewer in number and distributed preferentially toward the nuclear interior (Fig. 5b(iii) and (iv)). These findings underscore the biophysical mechanism by which the linear crosslink profile, coupled with contractile motor activity, promotes chromatin compaction and heterochromatin formation at the nuclear periphery. Contractile motors locally reinforce crosslink density, restricting chromatin mobility and facilitating the formation of dense chromatin domains. This process drives the segregation of heterochromatin at the periphery, while less dense euchromatin remains enriched at the nuclear interior.

To further examine the coupling between motor localization, crosslink enrichment, and chromatin density, we generate 2D colormaps of local chromatin density, ϕ^{c}_{local}, as a function of nuclear radius (R_s) and local crosslink number per motor (N^{m}_{c}) for each motor. In the linear crosslink profile, chromatin density increases with N^{m}_{c}, particularly in the outer nuclear regions. Contractile motors exhibit stronger compaction – reflected by higher ϕ^{c}_{local} – towards the peripheral nuclear regions with increased N^{m}_{c}, consistent with their role in promoting local chromatin compaction (Fig. 6(a) and (b)). For the inverted crosslink profile (bottom row), the density distribution shifts toward the nuclear interior, consistent with higher crosslink concentration near the center. Motors with higher N^{m}_{c} again associate with locally compact chromatin, but this effect is more localized to the central region. This spatial dependence highlights that high chromatin density is found at regions with more crosslinks per motor, which in part, reflects the underlying radial profile of chromatin crosslinks (Fig. 6(d) and (e)).

Consistent with the above findings, snapshots of the local neighborhoods surrounding contractile and extensile motors with maximum and minimum crosslinks for both linear (Fig. 6c) and inverted crosslink profiles (Fig. 6f) support our observations. Contractile motors with the maximum observed number of crosslinks exhibit the highest local crowding of chromatin (Fig. 6c(iii)), while extensile motors with minimal crosslinking display a significantly more sparse local environment (Fig. 6c(ii)). These data further support the coupling of motor activity with local crosslinking density as a mechanism for driving and sustaining spatially varying chromatin density.

D. Nuclear deformation correlates with peripheral chromatin compaction

Alterations to chromatin organization and localization at the nuclear periphery are closely linked to changes in nuclear shape, as reported in earlier studies.[59,73,75,78,89–92] Peripheral chromatin compaction along with chromatin–lamina linkages are thought to induce dynamic deformations of the nuclear envelope.[23,58] Hence, we quantitatively analyze the shape fluctuations of the soft nuclear lamina in our model. We first measure these fluctuations by measuring radial deviations of local heights across cross-sections of the approximately spherical shell, and compute the corresponding power spectrum of surface undulations (Fig. S8).[23,57,58,72,82] For each time frame, the center of mass of the nuclear lamina is first determined, along with the average radius, $\langle R_s \rangle$. Heights of monomers, corresponding to local fluctuations are given by the difference between their radial positions and $\langle R_s \rangle$. We take regions of three or more lamina monomers to constitute local deformations, which we classify into two distinct types: outward

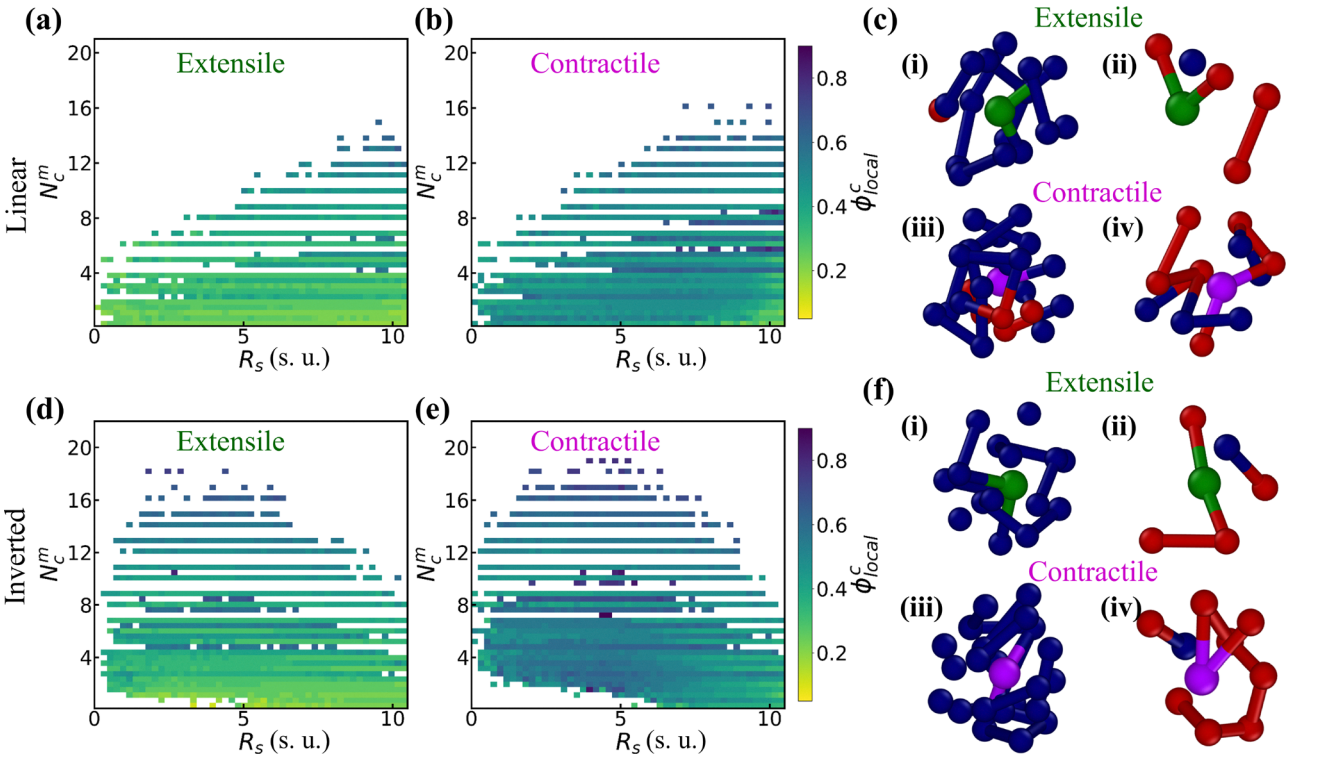

Fig. 6 Motor–crosslink coupling modulates local chromatin density for linear and inverted crosslink profiles. Colormap of local chromatin density (ϕ^{c}_{local}) as a function of nuclear radius (R_s) and number of crosslinks per motor (N^{m}_{c}) for extensile and contractile motors for linear (top row: (a) and (b)) and inverted (bottom row: (d) and (e)) crosslink profiles. The color bar represents the normalized local chromatin density. Panels (c) and (f) show the local neighborhoods of an extensile motor (i) and (ii) and a contractile motor (iii) and (iv), with maximum and minimum crosslinks, respectively, for linear (top row) and reverse (bottom row) profiles. Magenta/green: contractile/extensile motors; blue: crosslinked chromatin; red: chromatin monomers. All quantities are reported in simulation units (s.u.), where 1 s.u. of length = 1 μm and 1 s.u. of time = 0.5 s.

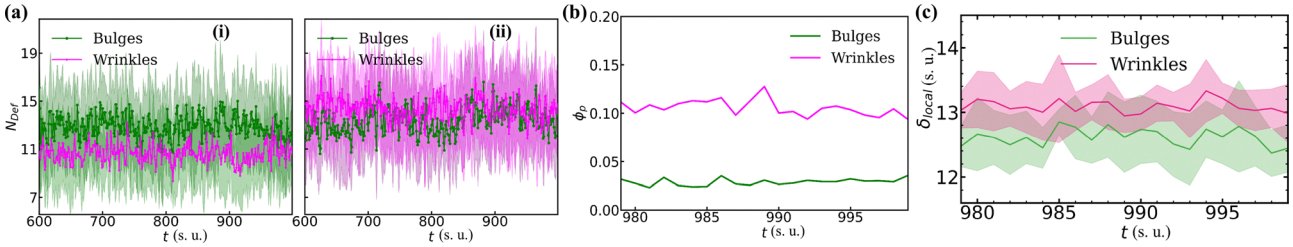

Fig. 7 Temporal profile of nuclear deformations and local properties of bulges and wrinkles with motor activity for a linear crosslink profile. Time evolution of (a) the number of bulges/wrinkles (N_{def}) for (i) extensile and (ii) contractile motors, (b) chromatin density (ϕ_p) at bulges/wrinkles, and (c) local fluctuations (δ_{local}) characterizing bulges and wrinkle regions, all for a linear crosslink density profile. The results shown correspond to N_c = 2000 crosslinks and N_L = 600 chromatin–lamina linkages. All quantities are reported in simulation units (s.u.), where 1 s.u. of length = 1 μm and 1 s.u. of time = 0.5 s. The shaded regions represent the standard error of the mean, calculated over 50 independent configurations.

protrusions, referred to as bulges, and inward indentations, termed wrinkles. A contiguous region is taken as a bulge or wrinkle if it deviates from the average radius by >10%, with positive and negative deviations identified as bulges and wrinkles, respectively.

To quantify the mechanical response of the deformed regions, we evaluate the local monomer positional fluctuations for bulges and wrinkles. These local fluctuations are quantified as the standard deviation of distances from each monomer in the bulge or wrinkle to their respective local center of mass. The parameter δ_{local} is defined as the inverse of the mean squared fluctuation. Higher values of δ_{local} indicate regions with smaller deformations. Over long times, larger δ_{local} suggests greater local resistance to deformation, and therefore stiffer areas of the nuclear periphery, while lower values may correspond to more flexible regions.

In Fig. 7, we plot the time evolution of the number, N_{Def}, of deformations, the chromatin density at these deformation sites, and the local fluctuations, δ_{local}, associated with the bulges/wrinkles for the linear crosslink profile. The time series of N_{Def} reveals that contractile motors induce more deformations, particularly wrinkles, compared to extensile motors (Fig. 7a). In addition, the polymer density at these deformation sites in the case of contractile motors indicates a greater localization of chromatin within the wrinkles compared to the bulges (Fig. 7b). This observation is supported by the time series of the inverse-squared fluctuation, δ_{local}, which is consistently larger for wrinkles, suggesting higher stiffness, compared to bulges (Fig. 7c). The elevated stiffness of the wrinkles is consistent with prior experimental investigations of the mechanical response of the cell nucleus to external forces, which found that nuclear envelope restructuring characterized by wrinkle unfolding is associated with instantaneous stiffening of the nucleus under applied indentation.[73]

IV. Discussion

We have analyzed how crosslink distribution and motor activity collectively influence chromatin spatial organization, promoting preferential peripheral heterochromatin formation and resulting in a spatially segregated architecture resembling conventional nuclear organization. This behavior is captured by our computational model, in which the lamina is represented as a soft deformable sphere and chromatin as a crosslinked polymer chain tethered to the lamina, with dynamic motor proteins driving emergent chromatin compartmentalization. Differential density segregation is driven by the interplay of spatial constraints on chromatin – chromatin–lamina linkages and crosslinking – and the highly correlated local polymer dynamics driven by the molecular motors. The specific spatial distribution of crosslinks within the nuclear volume plays a critical role in regulating both the location and degree of chromatin compaction, and can result in either conventional or inverted 3D genome architectures. Contractile motors in particular amplify these effects by promoting the formation of dense chromatin domains, particularly in regions of dense crosslinking. Chromatin organization in this model is coupled to deformations of the nuclear lamina, with wrinkling in particular correlated with chromatin accumulation at the periphery. We hypothesize that chromatin accumulation could lead to feedback that self-reinforces peripheral heterochromatin organization, and therefore, dynamically and adaptively modulates nuclear mechanical response.

The spatially varying crosslinking profile is critical to the nonequilibrium mechanism that generates and sustains nonuniform chromatin densities. It is only with the linear crosslinking profile that we observe conventional nuclear organization of dense peripheral chromatin with less dense interior chromatin. Nonetheless, motor activity is essential, as this density contrast does not arise in the passive system. However, motor activity need not be heterogeneous as assumed in previous models of nonequilibrium mechanisms of chromatin compartmentalization;[37,38,41,43–46] our model implements activity that is distributed uniformly across the chromatin polymer fiber.

Our local density-based classification approach, measuring densities of heterochromatin and euchromatin, demonstrates that this mechanism can achieve experimentally observed differences in density. We find approximately 50% difference in the densities of heterochromatin and euchromatin, consistent with values reported from both differential interference contrast and electron microscopy.[6,7] The density difference arises from motors employed in our model, with contractile motors markedly elevating the number of crosslinks per motor

in their vicinity, resulting in recruitment of chromatin and strongly constrained local chromatin motion. The self-reinforcing nature of this mechanism forms and sustains the high-density heterochromatin domains and that accumulate near the nuclear periphery in conventional nuclear organization.

The soft nuclear lamina exhibits dynamic shape fluctuations, as reported in previous studies,[57,58,72,73,78,93] and these deformations can give rise to the formation of bulges and wrinkles.[73] Wrinkles formed in the presence of contractile motors exhibit greater apparent stiffness than bulges, and they are correlated with a higher local concentration of chromatin. These observations raise the possibility of an adapative mechanism, whereby externally applied forces that induce wrinkling can locally increase chromatin density. This could lead to further recruitment of chromatin by the active mechanism described in this work, which would locally and dynamically stiffen the nuclear periphery. Beyond static deformations, our model also captures dynamic fluctuations of the nuclear shape. These fluctuations can be probed experimentally by perturbing motor activity or chromatin–lamina coupling, such as through ATP depletion, blebbistatin treatment, or disruption of cytoskeletal linkers such as the LINC complex-which should suppress the low-frequency enhancement if driven by active stresses. Similar behavior was observed by Chu *et al.*, where ATP depletion reduced low-frequency nuclear undulations,[57] in agreement with our findings.

To experimentally validate our model's predictions on the role of spatially patterned crosslinks and motor activity in shaping nuclear chromatin organization, we propose combining high-resolution chromatin imaging with genetic perturbations. The crosslink distribution can be visualized *via* immunofluorescence of endogenous proteins, such as HP1α/γ, that crosslink chromatin and mark heterochromatin-associated domains.[6,94] Crosslink density can be modulated by tuning HP1 expression levels: overexpression could promote chromatin crosslinking *via* HP1 oligomerization espeically in H3K9me3-enriched regions, while depletion or mutation would reduce crosslink formation.[11,12,66,95] Spatially patterned crosslinking could potentially be genetically engineered through synthetic recruitment of HP1 to defined genomic loci[96,97] or optogenetically induced clustering,[98,99] enabling spatial modulation of local crosslink density. Motor activity may be experimentally modulated by altering ATP availability or treating with inhibitors of transcription and other active processes.[49] Locus tracking[51,100] can assess the dynamic impact of crosslinks and motors. Together, these approaches provide a versatile framework to test the mechanistic hypotheses emerging from our simulations.

Conflicts of interest

There are no conflicts to declare.

Data availability

The data supporting this article have been included as part of the supplementary information (SI). The SI contains detailed simulation parameters and additional analyses, including chromatin density profiles illustrating the effects of chromatin-lamina linkages and motor-number dependence, as well as analyses of nuclear lamina shape fluctuations. See DOI: https://doi.org/10.1039/d5sm00812c.

The datasets supporting this article are available from the corresponding author upon reasonable request.

Acknowledgements

This research was supported in part through computational resources provided by Syracuse University. EJB acknowledges support from the NIH Common Fund 4D Nucleome Program (UM1HG011536). JMS acknowledges funding support from the National Science Foundation under grant DMR-2204312.

References

1 T. Misteli, The self-organizing genome: principles of genome architecture and function, *Cell*, 2020, **183**, 28.
2 Y. Kalukula, A. D. Stephens, J. Lammerding and S. Gabriele, Mechanics and functional consequences of nuclear deformations, *Nat. Rev. Mol. Cell Biol.*, 2022, **23**, 583.
3 I. Solovei, K. Thanisch and Y. Feodorova, How to rule the nucleus: divide et impera, *Curr. Opin. Cell Biol.*, 2016, **40**, 47.
4 J. Dekker and L. A. Mirny, The chromosome folding problem and how cells solve it, *Cell*, 2024, **187**, 6424.
5 I. Solovei, M. Kreysing, C. Lanctôt, S. Kösem, L. Peichl, T. Cremer, J. Guck and B. Joffe, Nuclear architecture of rod photoreceptor cells adapts to vision in mammalian evolution, *Cell*, 2009, **137**, 356.
6 R. Imai, T. Nozaki, T. Tani, K. Kaizu, K. Hibino, S. Ide, S. Tamura, K. Takahashi, M. Shribak and K. Maeshima, Density imaging of heterochromatin in live cells using orientation-independent-DIC microscopy, *Mol. Biol. Cell*, 2017, **28**, 3349.
7 H. D. Ou, S. Phan, T. J. Deerinck, A. Thor, M. H. Ellisman and C. C. O'shea, Chromemt: Visualizing 3D chromatin structure and compaction in interphase and mitotic cells, *Science*, 2017, **357**, eaag0025.
8 M. Barbieri, M. Chotalia, J. Fraser, L.-M. Lavitas, J. Dostie, A. Pombo and M. Nicodemi, Complexity of chromatin folding is captured by the strings and binders switch model, *Proc. Natl. Acad. Sci. U. S. A.*, 2012, **109**, 16173.
9 D. Jost, P. Carrivain, G. Cavalli and C. Vaillant, Modeling epigenome folding: formation and dynamics of topologically associated chromatin domains, *Nucleic Acids Res.*, 2014, **42**, 9553.
10 M. Di Pierro, B. Zhang, E. L. Aiden, P. G. Wolynes and J. N. Onuchic, Transferable model for chromosome architecture, *Proc. Natl. Acad. Sci. U. S. A.*, 2016, **113**, 12168.
11 A. G. Larson, D. Elnatan, M. M. Keenen, M. J. Trnka, J. B. Johnston, A. L. Burlingame, D. A. Agard, S. Redding and G. J. Narlikar, Liquid droplet formation by HP1α

suggests a role for phase separation in heterochromatin, *Nature*, 2017, **547**, 236.
12 A. R. Strom, A. V. Emelyanov, M. Mir, D. V. Fyodorov, X. Darzacq and G. H. Karpen, Phase separation drives heterochromatin domain formation, *Nature*, 2017, **547**, 241.
13 S. S. Rao, S.-C. Huang, B. G. St Hilaire, J. M. Engreitz, E. M. Perez, K.-R. Kieffer-Kwon, A. L. Sanborn, S. E. Johnstone, G. D. Bascom and I. D. Bochkov, *et al.*, Cohesin loss eliminates all loop domains, *Cell*, 2017, **171**, 305.
14 J. Nuebler, G. Fudenberg, M. Imakaev, N. Abdennur and L. A. Mirny, Chromatin organization by an interplay of loop extrusion and compartmental segregation, *Proc. Natl. Acad. Sci. U. S. A.*, 2018, **115**, E6697.
15 M. Falk, Y. Feodorova, N. Naumova, M. Imakaev, B. R. Lajoie, H. Leonhardt, B. Joffe, J. Dekker, G. Fudenberg and I. Solovei, *et al.*, Heterochromatin drives compartmentalization of inverted and conventional nuclei, *Nature*, 2019, **570**, 395.
16 B. A. Gibson, L. K. Doolittle, M. W. Schneider, L. E. Jensen, N. Gamarra, L. Henry, D. W. Gerlich, S. Redding and M. K. Rosen, Organization of chromatin by intrinsic and regulated phase separation, *Cell*, 2019, **179**, 470.
17 L. Wang, Y. Gao, X. Zheng, C. Liu, S. Dong, R. Li, G. Zhang, Y. Wei, H. Qu and Y. Li, *et al.*, Histone modifications regulate chromatin compartmentalization by contributing to a phase separation mechanism, *Mol. Cell*, 2019, **76**, 646.
18 S. Sanulli, M. Trnka, V. Dharmarajan, R. Tibble, B. Pascal, A. Burlingame, P. Griffin, J. Gross and G. Narlikar, HP1 reshapes nucleosome core to promote phase separation of heterochromatin, *Nature*, 2019, **575**, 390.
19 D. Amiad-Pavlov, D. Lorber, G. Bajpai, A. Reuveny, F. Roncato, R. Alon, S. Safran and T. Volk, Live imaging of chromatin distribution reveals novel principles of nuclear architecture and chromatin compartmentalization, *Sci. Adv.*, 2021, **7**, eabf6251.
20 O. Adame-Arana, G. Bajpai, D. Lorber, T. Volk and S. Safran, Regulation of chromatin microphase separation by binding of protein complexes, *eLife*, 2023, **12**, e82983.
21 L. A. Mirny, M. Imakaev and N. Abdennur, Two major mechanisms of chromosome organization, *Curr. Opin. Cell Biol.*, 2019, **58**, 142.
22 G. Bajpai, D. Amiad Pavlov, D. Lorber, T. Volk and S. Safran, Mesoscale phase separation of chromatin in the nucleus, *eLife*, 2021, **10**, e63976.
23 A. G. Attar, J. Paturej, E. J. Banigan and A. Erbas, Chromatin phase separation and nuclear shape fluctuations are correlated in a polymer model of the nucleus, *Nucleus*, 2024, **15**, 2351957.
24 D. Michieletto, E. Orlandini and D. Marenduzzo, Polymer model with epigenetic recoloring reveals a pathway for the de novo establishment and 3D organization of chromatin domains, *Phys. Rev. X*, 2016, **6**, 041047.
25 D. Michieletto, D. Col, D. Marenduzzo and E. Orlandini, Nonequilibrium theory of epigenomic microphase separation in the cell nucleus, *Phys. Rev. Lett.*, 2019, **123**, 228101.
26 J. A. Owen, D. Osmanović and L. Mirny, Design principles of 3D epigenetic memory systems, *Science*, 2023, **382**, eadg3053.
27 S. E. Murphy and A. N. Boettiger, Polycomb repression of Hox genes involves spatial feedback but not domain compaction or phase transition, *Nat. Genet.*, 2024, **56**, 493.
28 G. Spracklin, N. Abdennur, M. Imakaev, N. Chowdhury, S. Pradhan, L. A. Mirny and J. Dekker, Diverse silent chromatin states modulate genome compartmentalization and loop extrusion barriers, *Nat. Struct. Mol. Biol.*, 2023, **30**, 38.
29 S. S. Rao, M. H. Huntley, N. C. Durand, E. K. Stamenova, I. D. Bochkov, J. T. Robinson, A. L. Sanborn, I. Machol, A. D. Omer and E. S. Lander, *et al.*, A 3D map of the human genome at kilobase resolution reveals principles of chromatin looping, *Cell*, 2014, **159**, 1665.
30 S. Ghosh, V. C. Cuevas, B. Seelbinder and C. P. Neu, Image-based elastography of heterochromatin and euchromatin domains in the deforming cell nucleus, *Small*, 2021, **17**, 2006109.
31 P. R. Cook and D. Marenduzzo, Entropic organization of interphase chromosomes, *J. Cell Biol.*, 2009, **186**, 825.
32 A. Brunet, N. Destainville and P. Collas, Physical constraints in polymer modeling of chromatin associations with the nuclear periphery at kilobase scale, *Nucleus*, 2021, **12**, 6.
33 M. Girard, M. O. De La Cruz, J. F. Marko and A. Erbaş, Heterogeneous flexibility can contribute to chromatin segregation in the cell nucleus, *Phys. Rev. E*, 2024, **110**, 014403.
34 A. Buckle, C. A. Brackley, S. Boyle, D. Marenduzzo and N. Gilbert, Polymer simulations of heteromorphic chromatin predict the 3D folding of complex genomic loci, *Mol. Cell*, 2018, **72**, 786.
35 C. A. Brackley, S. Taylor, A. Papantonis, P. R. Cook and D. Marenduzzo, Nonspecific bridging-induced attraction drives clustering of DNA-binding proteins and genome organization, *Proc. Natl. Acad. Sci. U. S. A.*, 2013, **110**, E3605.
36 C. A. Brackley, J. Johnson, S. Kelly, P. R. Cook and D. Marenduzzo, Simulated binding of transcription factors to active and inactive regions folds human chromosomes into loops, rosettes and topological domains, *Nucleic Acids Res.*, 2016, **44**, 3503.
37 N. Ganai, S. Sengupta and G. I. Menon, Chromosome positioning from activity-based segregation, *Nucleic Acids Res.*, 2014, **42**, 4145.
38 A. Y. Grosberg and J.-F. Joanny, Nonequilibrium statistical mechanics of mixtures of particles in contact with different thermostats, *Phys. Rev. E:Stat., Nonlinear, Soft Matter Phys.*, 2015, **92**, 032118.
39 J. Smrek and K. Kremer, Small activity differences drive phase separation in active-passive polymer mixtures, *Phys. Rev. Lett.*, 2017, **118**, 098002.
40 L. Liu, G. Shi, D. Thirumalai and C. Hyeon, Chain organization of human interphase chromosome determines the

spatiotemporal dynamics of chromatin loci, *PLoS Comput. Biol.*, 2018, **14**, e1006617.
41 R. Das, T. Sakaue, G. Shivashankar, J. Prost and T. Hiraiwa, How enzymatic activity is involved in chromatin organization, *eLife*, 2022, **11**, e79901.
42 S. Chaki, L. Theeyancheri and R. Chakrabarti, A polymer chain with dipolar active forces in connection to spatial organization of chromatin, *Soft Matter*, 2023, **19**, 1348.
43 A. Mahajan, W. Yan, A. Zidovska, D. Saintillan and M. J. Shelley, Euchromatin activity enhances segregation and compaction of heterochromatin in the cell nucleus, *Phys. Rev. X*, 2022, **12**, 041033.
44 L. Hilbert, Y. Sato, K. Kuznetsova, T. Bianucci, H. Kimura, F. Jülicher, A. Honigmann, V. Zaburdaev and N. L. Vastenhouw, Transcription organizes euchromatin *via* microphase separation, *Nat. Commun.*, 2021, **12**, 1360.
45 S. Brahmachari, T. Markovich, F. C. MacKintosh and J. N. Onuchic, Temporally correlated active forces drive segregation and enhanced dynamics in chromosome polymers, *PRX Life*, 2024, **2**, 033003.
46 A. Goychuk, D. Kannan, A. K. Chakraborty and M. Kardar, Polymer folding through active processes recreates features of genome organization, *Proc. Natl. Acad. Sci. U. S. A.*, 2023, **120**, e2221726120.
47 J. Smrek, I. Chubak, C. N. Likos and K. Kremer, Active topological glass, *Nat. Commun.*, 2020, **11**, 26.
48 I. Chubak, S. M. Pachong, K. Kremer, C. N. Likos and J. Smrek, Active topological glass confined within a spherical cavity, *Macromolecules*, 2022, **55**, 956.
49 A. Zidovska, D. A. Weitz and T. J. Mitchison, Micron-scale coherence in interphase chromatin dynamics, *Proc. Natl. Acad. Sci. U. S. A.*, 2013, **110**, 15555.
50 H. A. Shaban, R. Barth and K. Bystricky, Formation of correlated chromatin domains at nanoscale dynamic resolution during transcription, *Nucleic Acids Res.*, 2018, **46**, e77.
51 N. Khanna, Y. Zhang, J. S. Lucas, O. K. Dudko and C. Murre, Chromosome dynamics near the sol-gel phase transition dictate the timing of remote genomic interactions, *Nat. Commun.*, 2019, **10**, 2771.
52 R. Barth, K. Bystricky and H. Shaban, Coupling chromatin structure and dynamics by live super-resolution imaging, *Sci. Adv.*, 2020, **6**, eaaz2196.
53 H. A. Shaban, R. Barth, L. Recoules and K. Bystricky, Hi-D: nanoscale mapping of nuclear dynamics in single living cells, *Genome Biol.*, 2020, **21**, 95.
54 I. Eshghi, J. A. Eaton and A. Zidovska, Interphase chromatin undergoes a local sol-gel transition upon cell differentiation, *Phys. Rev. Lett.*, 2021, **126**, 228101.
55 M. Locatelli, J. Lawrimore, H. Lin, S. Sanaullah, C. Seitz, D. Segall, P. Kefer, N. Salvador Moreno, B. Lietz and R. Anderson, *et al.*, DNA damage reduces heterogeneity and coherence of chromatin motions, *Proc. Natl. Acad. Sci. U. S. A.*, 2022, **119**, e2205166119.
56 R. Bruinsma, A. Y. Grosberg, Y. Rabin and A. Zidovska, Chromatin hydrodynamics, *Biophys. J.*, 2014, **106**, 1871.
57 F.-Y. Chu, S. C. Haley and A. Zidovska, On the origin of shape fluctuations of the cell nucleus, *Proc. Natl. Acad. Sci. U. S. A.*, 2017, **114**, 10338.
58 K. Liu, A. E. Patteson, E. J. Banigan and J. Schwarz, Dynamic nuclear structure emerges from chromatin cross-links and motors, *Phys. Rev. Lett.*, 2021, **126**, 158101.
59 I. K. Berg, M. L. Currey, S. Gupta, Y. Berrada, B. V. Nguyen, M. Pho, A. E. Patteson, J. Schwarz, E. J. Banigan and A. D. Stephens, Transcription inhibition suppresses nuclear blebbing and rupture independently of nuclear rigidity, *J. Cell Sci.*, 2023, **136**, jcs261547.
60 K. Prince, K. Lin, A. Li, N. Borowski and A. D. Stephens, Transcriptional activity generates chromatin motion that drives nuclear blebbing, *bioRxiv*, 2025, preprint, DOI: 10.1101/2025.05.20.655131.
61 A. Zidovska, The self-stirred genome: large-scale chromatin dynamics, its biophysical origins and implications, *Curr. Opin. Genet. Dev.*, 2020, **61**, 83.
62 A. Bird, Cohesin as an essential disruptor of chromosome organization, *Mol. Cell*, 2025, **85**, 1054.
63 D. Canzio, E. Y. Chang, S. Shankar, K. M. Kuchenbecker, M. D. Simon, H. D. Madhani, G. J. Narlikar and B. Al-Sady, Chromodomain-mediated oligomerization of HP1 suggests a nucleosome-bridging mechanism for heterochromatin assembly, *Mol. Cell*, 2011, **41**, 67.
64 D. Canzio, A. Larson and G. J. Narlikar, Mechanisms of functional promiscuity by HP1 proteins, *Trends Cell Biol.*, 2014, **24**, 377.
65 S. Machida, Y. Takizawa, M. Ishimaru, Y. Sugita, S. Sekine, J.-I. Nakayama, M. Wolf and H. Kurumizaka, Structural basis of heterochromatin formation by human HP1, *Mol. Cell*, 2018, **69**, 385.
66 A. R. Strom, R. J. Biggs, E. J. Banigan, X. Wang, K. Chiu, C. Herman, J. Collado, F. Yue, J. C. Ritland Politz and L. J. Tait, *et al.*, HP1α is a chromatin crosslinker that controls nuclear and mitotic chromosome mechanics, *eLife*, 2021, **10**, e63972.
67 V. Sokolova, J. Miratsky, V. Svetlov, M. Brenowitz, J. Vant, T. S. Lewis, K. Dryden, G. Lee, S. Sarkar and E. Nudler, *et al.*, Structural mechanism of HP1α-dependent transcriptional repression and chromatin compaction, *Structure*, 2024, **32**, 2094.
68 A. Kumar and H. Kono, Heterochromatin protein 1 (HP1): interactions with itself and chromatin components, *Biophys. Rev.*, 2020, **12**, 387.
69 Y. Yang, R. Liu, R. Qiu, Y. Zheng, W. Huang, H. Hu, Q. Ji, H. He, Y. Shang and Y. Gong, *et al.*, CRL4B promotes tumorigenesis by coordinating with SUV39H1/HP1/DNMT3A in DNA methylation-based epigenetic silencing, *Oncogene*, 2015, **34**, 104.
70 D. Saintillan, M. J. Shelley and A. Zidovska, Extensile motor activity drives coherent motions in a model of interphase chromatin, *Proc. Natl. Acad. Sci. U. S. A.*, 2018, **115**, 11442.

71 S. Redding, Dynamic asymmetry and why chromatin defies simple physical definitions, *Curr. Opin. Cell Biol.*, 2021, **70**, 116.
72 A. E. Patteson, A. Vahabikashi, K. Pogoda, S. A. Adam, K. Mandal, M. Kittisopikul, S. Sivagurunathan, A. Goldman, R. D. Goldman and P. A. Janmey, Vimentin protects cells against nuclear rupture and DNA damage during migration, *J. Cell Biol.*, 2019, **218**, 4079.
73 W. Tang, X. Chen, X. Wang, M. Zhu, G. Shan, T. Wang, W. Dou, J. Wang, J. Law and Z. Gong, *et al.*, Indentation induces instantaneous nuclear stiffening and unfolding of nuclear envelope wrinkles, *Proc. Natl. Acad. Sci. U. S. A.*, 2023, **120**, e2307356120.
74 A. Tajik, Y. Zhang, F. Wei, J. Sun, Q. Jia, W. Zhou, R. Singh, N. Khanna, A. S. Belmont and N. Wang, Transcription upregulation *via* force-induced direct stretching of chromatin, *Nat. Mater.*, 2016, **15**, 1287.
75 A. D. Stephens, E. J. Banigan and J. F. Marko, Chromatin's physical properties shape the nucleus and its functions, *Curr. Opin. Cell Biol.*, 2019, **58**, 76.
76 M. M. Nava, Y. A. Miroshnikova, L. C. Biggs, D. B. Whitefield, F. Metge, J. Boucas, H. Vihinen, E. Jokitalo, X. Li and J. M. G. Arcos, *et al.*, Heterochromatin-driven nuclear softening protects the genome against mechanical stress-induced damage, *Cell*, 2020, **181**, 800.
77 C.-R. Hsia, J. McAllister, O. Hasan, J. Judd, S. Lee, R. Agrawal, C.-Y. Chang, P. Soloway and J. Lammerding, Confined migration induces heterochromatin formation and alters chromatin accessibility, *iScience*, 2022, **25**, 104978.
78 H. Liang, Y.-J. Wang, Y. Liu, W. Liu, B. Liu and Y.-J. Liu, Microtopography-induced nuclear deformation triggers chromatin reorganization and cytoskeleton remodeling, *Chem. Biomed. Imaging*, 2024, **2**, 481.
79 A. G. Attar, J. Paturej, O. S. Sariyer, E. J. Banigan and A. Erbas, Peripheral heterochromatin tethering is required for chromatin-based nuclear mechanical response, *Nucleic Acids Res.*, 2025, **53**, gkaf763.
80 Y. A. Miroshnikova and S. A. Wickström, Mechanical forces in nuclear organization, *Cold Spring Harb Perspect Biol.*, 2022, **14**, a039685.
81 A. D. Stephens, E. J. Banigan, S. A. Adam, R. D. Goldman and J. F. Marko, Chromatin and lamin A determine two different mechanical response regimes of the cell nucleus, *Mol. Biol. Cell*, 2017, **28**, 1984.
82 E. J. Banigan, A. D. Stephens and J. F. Marko, Mechanics and buckling of biopolymeric shells and cell nuclei, *Biophys. J.*, 2017, **113**, 1654.
83 T. J. Kirby and J. Lammerding, Emerging views of the nucleus as a cellular mechanosensor, *Nat. Cell Biol.*, 2018, **20**, 373.
84 M. C. Lionetti, S. Bonfanti, M. R. Fumagalli, Z. Budrikis, F. Font-Clos, G. Costantini, O. Chepizhko, S. Zapperi and C. A. La Porta, Chromatin and cytoskeletal tethering determine nuclear morphology in progerin-expressing cells, *Biophys. J.*, 2020, **118**, 2319.
85 S. Shinkai, T. Nozaki, K. Maeshima and Y. Togashi, Dynamic nucleosome movement provides structural information of topological chromatin domains in living human cells, *PLoS Comput. Biol.*, 2016, **12**, e1005136.
86 K. Minami, K. Nakazato, S. Ide, K. Kaizu, K. Higashi, S. Tamura, A. Toyoda, K. Takahashi, K. Kurokawa and K. Maeshima, Replication-dependent histone labeling dissects the physical properties of euchromatin/heterochromatin in living human cells, *Sci. Adv.*, 2025, **11**, eadu8400.
87 N. A. Hathaway, O. Bell, C. Hodges, E. L. Miller, D. S. Neel and G. R. Crabtree, Dynamics and memory of heterochromatin in living cells, *Cell*, 2012, **149**, 1447.
88 T. Nozaki, R. Imai, M. Tanbo, R. Nagashima, S. Tamura, T. Tani, Y. Joti, M. Tomita, K. Hibino and M. T. Kanemaki, *et al.*, Dynamic organization of chromatin domains revealed by super-resolution live-cell imaging, *Mol. Cell*, 2017, **67**, 282.
89 A. Poleshko, K. M. Mansfield, C. C. Burlingame, M. D. Andrake, N. R. Shah and R. A. Katz, The human protein prr14 tethers heterochromatin to the nuclear lamina during interphase and mitotic exit, *Cell Rep.*, 2013, **5**, 292.
90 S. M. Schreiner, P. K. Koo, Y. Zhao, S. G. Mochrie and M. C. King, The tethering of chromatin to the nuclear envelope supports nuclear mechanics, *Nat. Commun.*, 2015, **6**, 7159.
91 A. D. Stephens, P. Z. Liu, E. J. Banigan, L. M. Almassalha, V. Backman, S. A. Adam, R. D. Goldman and J. F. Marko, Chromatin histone modifications and rigidity affect nuclear morphology independent of lamins, *Mol. Biol. Cell*, 2018, **29**, 220.
92 V. Introini, G. R. Kidiyoor, G. Porcella, P. Cicuta and M. Cosentino Lagomarsino, Centripetal nuclear shape fluctuations associate with chromatin condensation in early prophase, *Commun. Biol.*, 2023, **6**, 715.
93 S. Talwar, A. Kumar, M. Rao, G. I. Menon and G. Shivashankar, Correlated spatio-temporal fluctuations in chromatin compaction states characterize stem cells, *Biophys. J.*, 2013, **104**, 553.
94 B. Bintu, L. J. Mateo, J.-H. Su, N. A. Sinnott-Armstrong, M. Parker, S. Kinrot, K. Yamaya, A. N. Boettiger and X. Zhuang, Super-resolution chromatin tracing reveals domains and cooperative interactions in single cells, *Science*, 2018, **362**, eaau1783.
95 S. V. Brasher, B. O. Smith, R. H. Fogh, D. Nietlispach, A. Thiru, P. R. Nielsen, R. W. Broadhurst, L. J. Ball, N. V. Murzina and E. D. Laue, The structure of mouse HP1 suggests a unique mode of single peptide recognition by the shadow chromo domain dimer, *EMBO J.*, 2000, **19**, 1587–1597.
96 K. Ayyanathan, M. S. Lechner, P. Bell, G. G. Maul, D. C. Schultz, Y. Yamada, K. Tanaka, K. Torigoe and F. J. Rauscher, Regulated recruitment of HP1 to a euchromatic gene induces mitotically heritable, epigenetic gene silencing: a mammalian cell culture model of gene variegation, *Genes Dev.*, 2003, **17**, 1855.
97 P. J. Verschure, I. Van Der Kraan, W. De Leeuw, J. Van Der Vlag, A. E. Carpenter, A. S. Belmont and R. Van Driel,

In vivo HP1 targeting causes large-scale chromatin condensation and enhanced histone lysine methylation, *Mol. Cell. Biol.*, 2005, **25**, 4552.

98 Y. Shin, J. Berry, N. Pannucci, M. P. Haataja, J. E. Toettcher and C. P. Brangwynne, Spatiotemporal control of intracellular phase transitions using light-activated optodroplets, *Cell*, 2017, **168**, 159.

99 F. Erdel, A. Rademacher, R. Vlijm, J. Tünnermann, L. Frank, R. Weinmann, E. Schweigert, K. Yserentant, J. Hummert and C. Bauer, *et al.*, Mouse heterochromatin adopts digital compaction states without showing hallmarks of HP1-driven liquid-liquid phase separation, *Mol. Cell*, 2020, **78**, 236.

100 M. Gabriele, H. B. Brandão, S. Grosse-Holz, A. Jha, G. M. Dailey, C. Cattoglio, T.-H. S. Hsieh, L. Mirny, C. Zechner and A. S. Hansen, Dynamics of CTCF- and cohesin-mediated chromatin looping revealed by live-cell imaging, *Science*, 2022, **376**, 496.